

PAPER

## 2D selenium allotropes from first principles and swarm intelligence

To cite this article: Chao Liu *et al* 2019 *J. Phys.: Condens. Matter* **31** 235702

View the [article online](#) for updates and enhancements.



**IOP | ebooks™**

Bringing you innovative digital publishing with leading voices  
to create your essential collection of books in STEM research.

Start exploring the **collection** - download the first chapter of  
every title for free.

# 2D selenium allotropes from first principles and swarm intelligence

Chao Liu<sup>1,2</sup>, Tao Hu<sup>1,2</sup>, Yabei Wu<sup>1,2</sup>, Heng Gao<sup>1,2</sup>, Yali Yang<sup>1,2</sup>  
and Wei Ren<sup>1,2,3,4</sup>

<sup>1</sup> Department of Physics, and International Center of Quantum and Molecular Structures, Shanghai University, Shanghai 200444, People's Republic of China

<sup>2</sup> Materials Genome Institute and Shanghai Key Laboratory of High Temperature Superconductors, Shanghai University, Shanghai 200444, People's Republic of China

<sup>3</sup> State Key Laboratory of Solidification Processing, Northwestern Polytechnical University, Xi'an 710072, People's Republic of China

E-mail: [renwei@shu.edu.cn](mailto:renwei@shu.edu.cn)

Received 14 December 2018, revised 30 January 2019

Accepted for publication 8 February 2019


Published 29 March 2019



## Abstract

Combining the particle-swarm optimization method with first-principles calculations, we explore a new category of two-dimensional (2D) monolayers composed of solely the element selenium. Three stable structures are screened from outputs of crystal search computations, namely *T*-Se (1T-MoS<sub>2</sub>-like), *C*-Se (tiled 1D helical chain), and *S*-Se (square structure). Phonon calculations, as well as formation energy calculations have been performed to confirm the stability of the three phases. The electronic structure calculations show that both *T*-Se and *C*-Se are indirect-band-gap semiconductors, with gap values of 1.11 eV and 2.64 eV respectively when using the hybrid HSE06 functional. In particular, *C*-Se has a centrosymmetry-breaking structure which provides a spontaneous in-plane ferroelectric polarization of about  $2.68 \times 10^{-10} \text{ C m}^{-1}$  per layer. Interestingly, *S*-Se has a Dirac cone that can open up a band gap of 0.11 eV if spin-orbit coupling is included. The tilted Dirac cone of *S*-Se shows anisotropic band dispersion as characterized with different Fermi velocities of  $1.26 \times 10^6$  and  $0.24 \times 10^6 \text{ m s}^{-1}$  around the Dirac point. Our works enrich the family of 2D materials of selenium allotropes and show that their versatile properties could give rise to potential application in various fields.

Keywords: selenium allotropes, first principles, swarm intelligence, ferroelectric, Dirac cone, 2D materials

 Supplementary material for this article is available [online](#)

(Some figures may appear in colour only in the online journal)

## Introduction

Dimensionality is a crucial factor in determining fundamental properties besides the composition and arrangement of atoms in condensed matters [1]. Two-dimensional (2D) materials may possess unusual physical, chemical, optical and electronic properties than their bulk counterparts. In the last decade, 2D materials have attracted flourishing attention from both academia and industry [2–4]. The primary and

best known 2D material is graphene [5], after which various metallic and semiconducting 2D materials have been discovered, including transition metal dichalcogenides (TMDs) such as MoS<sub>2</sub> and WSe<sub>2</sub> [6, 7], hexagonal boron nitrides [8], group III to V elemental monolayers such as borophene, phosphorene and silicene [9–11], group III to IV chalcogenides such as GeS and InSe [12–14], and early transition metal carbides and carbonitrides (MXenes) such as Ti<sub>3</sub>C<sub>2</sub> [15] and V<sub>2</sub>C [16]. People believe that 2D layered materials can find potential applications in the fields of optoelectronics [17], spintronics [18], nanoelectronics [19, 20], energy storage

<sup>4</sup> Author to whom any correspondence should be addressed.

[21], and superconductor [22]. However, 2D materials functionality was seriously impeded by some disadvantages, for instance, lacking intrinsic band gap makes graphene difficult to be used in electronics [23], black phosphorus only conserves stability under special conditions [24], and many 2D materials consisting of group IV–VI elements have an indirect band gap [25]. Thus, it is necessary to explore even more novel 2D monolayers that have preeminent properties and can be exploited for specific applications.

Monolayer materials consisting of one single element are an important class of the 2D materials family. Up to now, in the field of single-element 2D materials, many elements have been explored. Besides graphene and phosphorene, elements that exist in the form of 2D structures also include boron [26, 27] in group-III, silicon [28], germanium [29], and stannum [30] in group-IV, and nitrogen [31], arsenic [32], antimony [33] and bismuth [34] in group-V, among them, the stannum and bismuth are metallic elements. Their 3D structures generally are layered with strong in-plane bonds and weak van der Waals coupling between layers, which allow the exfoliation of 2D materials with given number of layers from the bulk. Recently, Zhu *et al* have predicted and prepared tellurium-based monolayer materials, which supplemented the investigation of group-VI elemental monolayers [35]. Elements of group-VI and compounds of selenium and tellurium have been investigated previously. It is reported in the literature the syntheses of tellurium nanowires [36], tellurium nanotubes [37] and selenium nanosheet [38], but theoretical studies of such main group elemental selenium allotropes are still incomplete.

In this letter, we focus on single selenium elemental monolayers from prediction by using crystal structure searching method, and then the structural characteristics and corresponding electronic properties have been studied using first-principles calculations. Through phonon calculations, we show that Se-based monolayers can exist in the 1T-MoS<sub>2</sub>-like (*T*-Se) structure, tiled helical-chain (*C*-Se) and square (*S*-Se) structures. In great contrast to *T*-Se with centrosymmetry, *C*-Se has special non-centrosymmetric structure that is different from conventional 2D materials, which is formed with parallel 1D helical chains. We find that *C*-Se has a spontaneous in-plane ferroelectric polarization, and our electric charge analysis indicates the electrons transfer and hints a tendency of multivalence property. The band structure of *S*-Se has Dirac points and exhibits a band gap when including spin-orbital coupling (SOC). We calculate the band dispersion and Fermi velocity around the Dirac point to illustrate its tilted and anisotropic features. From the versatile properties of 2D selenium, we provide an outlook of future directions for research of these selenium-based monolayers, which could offer potential application in various fields.

## Computational details

### PSO calculations

As a global optimization method on a blind base, the particle-swarm optimization (PSO) algorithm was inspired by social behavior of bird flocking or fish schooling and can be viewed

**Table 1.** Structural parameters of 2D selenium obtained from DFT-TS method, together with the formation energy  $E_f$ . The formation energy is defined as  $E_f = E_{2D} - E_{bulk}$ , where  $E_{2D}$  is the total energy per atom of 2D selenium and  $E_{bulk}$  is the energy per atom of bulk selenium. The structural and energy properties of *bulk*-Se are also listed as a reference.

	Lattice constants (Å)	Bond length $d$ (Å)	Formation energy $E_f$ (eV/atom)
<i>T</i> -Se	$a = b = 3.74$	2.67	0.236
<i>C</i> -Se	$a = 4.99$ $b = 4.13$	$d_1 = 2.40$ $d_2 = 2.37$	0.122
<i>S</i> -Se	$a = b = 3.65$	$d_1 = 2.40$ $d_2 = 2.71$	0.264
<i>bulk</i> -Se	$a = b = 4.11$ $c = 5.16$	2.46	0

as a distributed-behavior algorithm that performs multidimensional search. PSO algorithm is fast and efficient to perform well on many optimization problems, and there are few parameters to adjust. We used the CALYPSO (Crystal structure AnaLYsis by Particle Swarm Optimization) code that is based on PSO technique within the evolutionary scheme and coupled with density functional theory (DFT) optimization to search for stable structures of 2D selenium [39]. In the PSO structural search, the number of generation is maintained at 20. All possible supercell sizes are considered with the total number of atoms no more than 12 in the supercell. That is, for 2D selenium, supercells with up to four unit-cells are considered. In the first generation, random structures are constructed by generating atomic coordinates using crystallographic symmetry operations. Next, the structures are optimized using a DFT method as detailed below. Then, the best 60% structures are selected by PSO to generate the next generation, and other structures in the new generation are generated randomly, which guarantee the structural diversity.

### DFT calculations

In the DFT simulations, we used the Vienna *ab initio* simulation package (VASP) [40, 41] to do the first-principles calculations. The generalized gradient approximation [42] within the Perdew–Burke–Ernzerhof (PBE) functional was employed to treat the exchange correlation interaction. The projector-augmented-wave potentials [43, 44] were implemented to describe the electron-ion interaction. The energy cutoff was selected to be 550 eV for the plane wave basis set. The Brillouin zones were set to  $15 \times 15 \times 1$   $k$ -grid mesh and sampled in the Monkhorst–Pack scheme. We set vacuum distance of 20 Å to avoid periodic interactions in  $z$  direction. The forces convergence standard on each atom was chosen as  $0.005 \text{ eV } \text{\AA}^{-1}$  and the self-consistent calculations were stopped until the energy difference was smaller than  $10^{-7}$  eV per atom. To make the band gap value close to experiments, the screened hybrid functional (HSE06) method [45, 46] was applied. In geometric optimization calculations, we used the PBE with different van der Waals (vdW) functionals (optB86b-vdW, optB88b-vdW, DFT-D3, DFT-D2, and

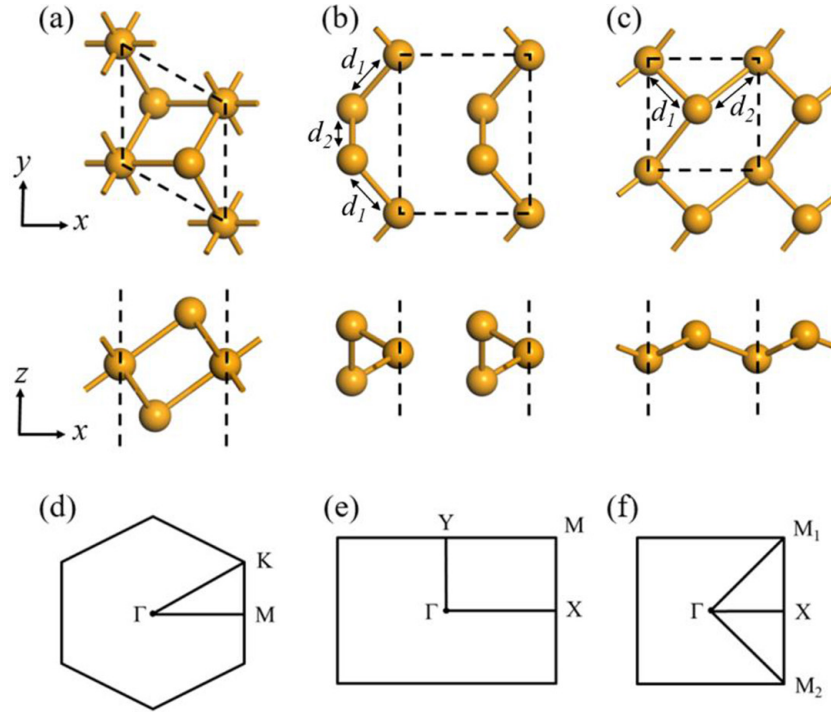


**Figure 1.** Top and side views of three optimized structures of 2D selenium: (a) *T*-Se, (b) *C*-Se, and (c) *S*-Se. The primitive cell of each phase was indicated by black dashed lines. The panels (d)–(f) are corresponding Brillouin zones, respectively. There are three atoms in each primitive cell for *T*-Se and *C*-Se, and two atoms for *S*-Se.

DFT-TS) to treat the long range interaction for the bulk selenium. It is proved that the DFT-TS functional is the best one to reproduce the experimental lattice constants. Therefore, the DFT-TS functional [47] is adopted in the optimization of the three monolayer phases.

#### Phonon spectra calculations

In the PSO structure search, each system is constrained within a range along the vacuum direction. This constraint is removed during the geometrical optimization in DFT calculations. Therefore, it is still conceivable that the predicted structures are not a local minimum due to the removal of the constraint and prefer to make larger buckling. To ensure predicted structures are local minima, we carry out phonon spectra calculations to examine the stability of all predicted low-energy structures. The phonon spectra are computed based on a DFT perturbation method with the PHONOPY package [48, 49]. We build a supercell of  $4 \times 4 \times 1$ , and the force criterion for ionic step is set to  $10^{-8}$  eV on each atom. Finally, we collect the structures with less imaginary phonon modes at  $\Gamma$  point and then distort positions of the atoms along the vibration eigenvectors of the zone center soft phonon mode to reach a stable structure. For the structures without imaginary modes, we raise the precision and confirm their stability again.

#### Results and discussion

We predicted three monolayer structures of selenium via PSO algorithm and denoted them as *T*-Se, *C*-Se, and *S*-Se. Their lattice parameters, bond lengths and formation energies per

atom are exhibited in table 1. Figure 1 shows the top and side views of optimized structures of these selenium monolayers which all have buckled structures. The *T*-phase in figure 1(a) has a 1T-MoS<sub>2</sub>-like sandwich structure, containing three Se atoms per unit cell. The atoms at different position have different bond numbers ( $N_b$ ) with the nearest neighbor atoms, such that the atoms in the middle of the sandwich structure have  $N_b = 6$ , while other two atoms in the upper and lower layers have  $N_b = 3$ . This feature is different from most of the single elemental monolayer materials that have same  $N_b$  for all atoms. The structure of *C*-Se consists of a series of 1D helical chains arranged on a plane as showed in figure 1(b). The weaker interactions of interchain atoms make helical chains tend to be independent of each other. Interestingly, the selenium nanosheets with *C*-phase structure have been synthesized experimentally and investigated for electronics and photonics applications. [38, 50] Furthermore, the *C*-phase has also been explored with new structures that have six atoms in a unit cell [51]. The monoclinic *S*-Se has only 2 atoms in a unit cell, and its lattice constants are  $a = b = 3.65$  Å as shown in figure 1(c). The structure of *S*-Se has a buckled configuration with one atom arranged at a corner of the square lattice. The other one atom is off the center of the square towards the corner direction. And the height difference of two atoms along out-of-plane direction is 0.78 Å. For *C*-Se and *S*-Se, we find their structures have symmetry breaking to gain stability, consequently both are low-symmetry systems.

Table 1 exhibits the detailed lattice parameters and formation energy ( $E_f$ ) of different Se allotropes. For *bulk*-Se, our calculated results by different vdW correction are displayed in figure S1 of the supplemental material ([stacks.iop.org/](https://stacks.iop.org/)

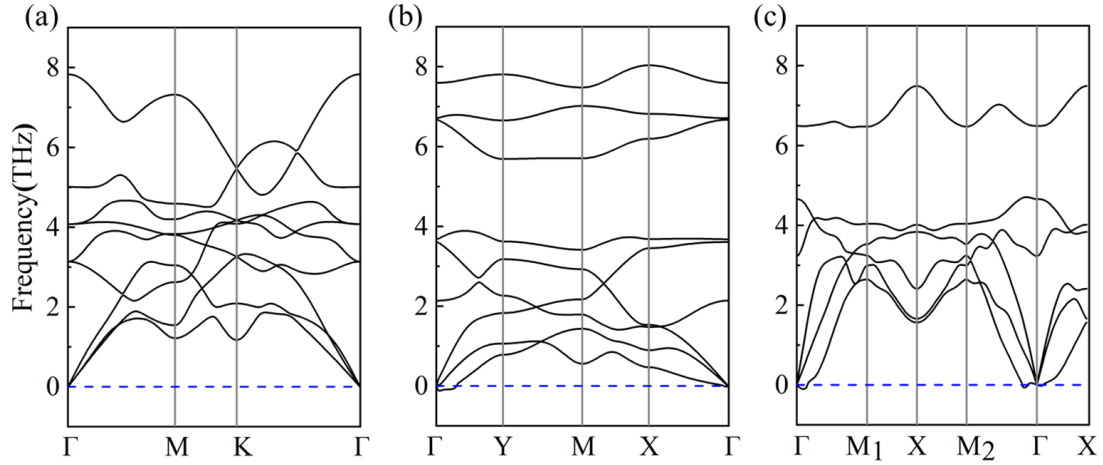


**Figure 2.** Phonon spectra of (a) *T*-Se, (b) *C*-Se and (c) *S*-Se, the special points have been mentioned in figure 1.

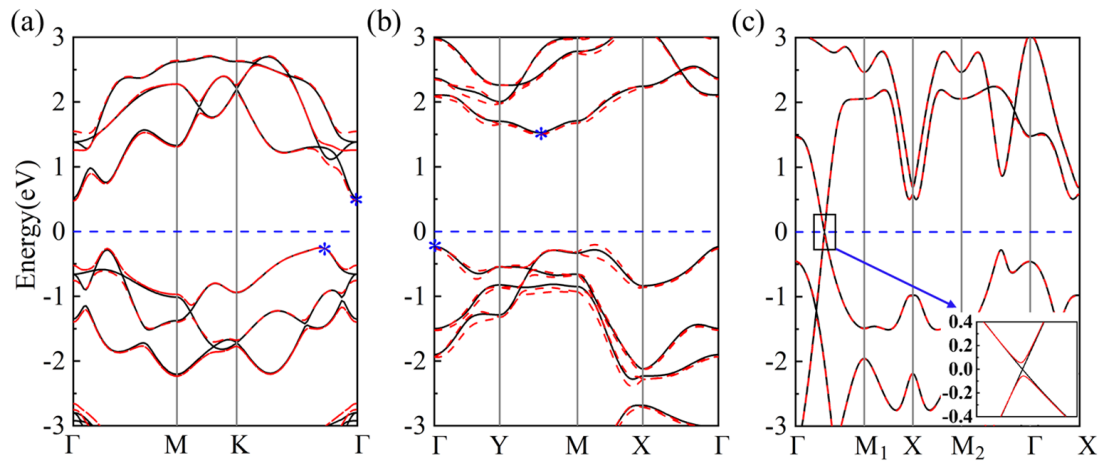


**Figure 3.** DFT-PBE band structures of (a) *T*-Se, (b) *C*-Se, and (c) *S*-Se without/with SOC effect are represented by the black solid and red dashed lines. The Fermi level is set to zero. The asterisks label the valence band maximum (VBM) and conduction band minimum (CBM). The inset in (c) is the zoom-in of the selected area of the band structure.

[JPhysCM/31/235702/mmedia](#)). The formation energy of the most stable *C*-Se is lower than that of the *T*-phase and *S*-phase by 0.114 eV and 0.142 eV per atom, respectively. For *C*-Se, its lattice parameters and bond lengths are close to those of *bulk*-Se because of its special structure composed of helical chains.

In the process of structure searching, we also obtained many interesting but less stable structures generated from CALYPSO, which are displayed and discussed in the Supplemental Material. Among them, we find two structures similar to the *T*-phase and *S*-phase, namely Meta-*T*-Se. For Meta-*T*-Se, its unit cell has three atoms, consisting a vertical square with 2.65 Å of side length, which has similar bond length of *T*-Se with 2.67 Å. It's worth mentioning that Meta-*T* phase has similar  $E_f$  than *T*-Se and the  $E_f$  even lower than that of *S*-Se. This structure may be stable under conditions of high temperature and/or in the presence of substrate.

The phonon calculations were performed to examine the structure stability of 2D selenium. The phonon spectra can identify the potential presence of soft phonon modes that may make structures unstable. Figure 2 shows the calculated phonon spectra of three phases of 2D selenium, it is obvious that phonon spectrum of *T*-Se is free of imaginary-frequency

**Table 2.** Band gaps of 2D selenium from the PBE (without/with SOC) and HSE06 (without/with SOC) methods.

	PBE	PBE+SOC	HSE	HSE+SOC (eV)
<i>T</i> -Se	0.71	0.67	1.11	1.04
<i>C</i> -Se	1.74	1.73	2.64	2.57
<i>S</i> -Se	0	0.11	0	0.12

phonon modes over the entire Brillouin zone, indicating this structure is stable in the freestanding form. The slight imaginary frequencies are seen in phonon spectra of *C*-Se and *S*-Se located near the  $\Gamma$  point. The corresponding atomic displacements can be followed in order to determine the stable phase. However, in a plane-wave DFT code like VASP, the exchange-correlation energies are computed on a discrete grid in the real space, and the uncertainty in phonon spectra per mode due to the numerically unresolved translational invariance is less than 0.1 THz in the systems considered [52, 53].

Band structures based on the PBE functional of *T*-Se, *C*-Se, and *S*-Se are plotted in figures 3(a)–(c), respectively. In addition, we also examine the effect of the SOC effect and show the results with red dashed lines. It is obvious that both



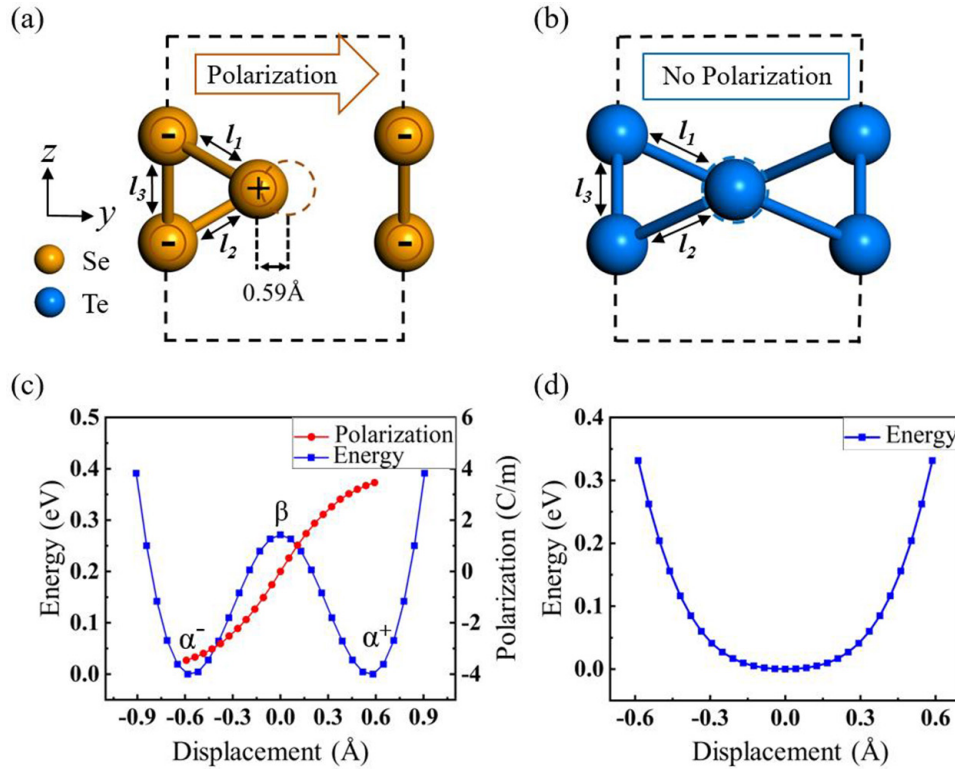


**Figure 4.** (a) The side views of polar C-Se (yellow atoms) with labeled positive and negative charge center by Bader charge analysis. The dashed circle indicates the nonpolar transition state. (b) The side views of centrosymmetric C-phase of tellurium (blue atoms). (c) The double-well potential and polarization-displacement relationship of C-Se. (d) The single potential well of C-phase of tellurium.

*T*-Se and *C*-Se are semiconductors and have indirect band gaps of  $E_g = 0.71 \text{ eV}$  and  $1.74 \text{ eV}$  respectively (see table 2). For *T*-Se, the  $k$  point position of valence band maximum (VBM) is between the  $\Gamma$  and  $K$  points while the conduction band minimum (CBM) is at  $\Gamma$  point. Besides, there appears another valence band peak along the  $\Gamma$  to  $M$  points, with a little lower energy than the VBM along  $\Gamma$ - $K$  direction. When the effect of SOC is considered, the band gap of *T*-Se is changed from non-SOC value  $0.71$  to  $0.67 \text{ eV}$ . The VBM and CBM of *C*-Se are located at  $\Gamma$  point and between  $X$  and  $M$  points, respectively. The band gap with SOC of *C*-Se is also reduced from non-SOC  $1.74 \text{ eV}$  to  $1.73 \text{ eV}$ . The band structure of *C*-Se shows a tendency of non-degenerate band splitting, which corresponds to its non-centrosymmetric structure. In order to remedy the potential deficiency that band calculation of DFT with local and semi-local functions underestimate the band gaps of semiconductors and insulators, we perform the band gap calculations with more accurate HSE06 hybrid functional (figure S2 of the supporting information) and display the band gap values in table 2. The HSE calculations generally shift down the valence bands and move up the conduction bands. Consequently, the band gap of  $1.11 \text{ eV}$  and  $2.64 \text{ eV}$  are obtained for *T*-Se and *C*-Se, and HSE+SOC calculations give slightly smaller band gaps. And the application of *T*-Se in optoelectronic field can be achieved with this gap value that is close to the band gap of bulk Si [54]. Notably, our calculations with HSE06 functional show that both *T*-Se and *C*-Se have different VBM positions from the results of PBE functional. The VBM position with HSE+SOC of *T*-Se is located at a peak between  $\Gamma$  and  $M$  points. And the VBM positions with

HSE and HSE+SOC of *C*-Se are located between  $X$  and  $M$  points and between  $M$  and  $Y$  points, respectively. However, overall the indirect band gaps are found for both PBE and HSE functionals, and for the cases that SOC is included.

In particular Se has a Dirac-cone-like band structure between the  $\Gamma$  and  $M_1$  points in the Brillouin zones indicated by a black box in figure 3(c). In the zoom-in, when SOC is not included in the band structure calculations, the band dispersion is linear in the  $\Gamma$ - $M_1$  direction near the Fermi level, and hence *S*-Se is a zero-gap semiconductor. When the SOC is included, *S*-Se exhibits a finite band gap with  $E_g = 0.11 \text{ eV}$ . Besides, we find the features of band structure from  $\Gamma$  to  $M_1$  and from  $\Gamma$  to  $M_2$  are similar to non-SOC result. From figure 1(c), the spatial symmetry is broken with the Se atom at the center of the square lattice displacing toward one of the square corners. The band structure appears to have anisotropic properties, which manifests that the band gap between  $\Gamma$  and  $M_2$  is much larger than that of  $\Gamma$ - $M_1$  direction.

We note that the structure of *C*-Se breaks the centrosymmetry, which is the necessary ingredient for a nonzero polarization. Bader charge analysis [55] is performed to investigate the charge transfer, we found that  $0.22$  electrons transfer from the pseudo-central atom to the two boundary atoms on the cross-section view as shown in figure 4(a). The pseudo-central Se atom behaves like to have positive charge while two boundary Se atoms show negatively charged. Therefore, the elemental monolayer of *C*-Se exhibits a spontaneous ferroelectric polarization. Further, as shown in figure 4(c), we calculated the energies with respect to the amplitude of atomic displacements. The two lowest energy points in the

double-well potential represent the aforementioned ground state ( $\alpha^+$  and  $\alpha^-$  with opposite polar directions). We have also used the nudged elastic band method [56, 57] to confirm its nonpolar transition state (i.e. the  $\beta$  at the saddle point of the energy curve) and find that the energy barrier between this double-well is about 271 meV per unit cell, and the amplitude of atom motion between  $\alpha$  and  $\beta$  phases is 0.59 Å as depicted by the open circle and solid atom in figure 4(a). Using the modern theory of polarization, i.e. Berry phase method [58, 59], we evaluate the spontaneous polarization for the ferroelectric  $\alpha$  phase. We find that polarization direction is along the  $y$ -axis, and its magnitude is about  $2.68 \times 10^{-10}$  C m $^{-1}$  per layer. This polarization value is much larger than those of some group-V elemental ferroelectric monolayers [60]. Such novel ferroelectric property of C-Se might be applied to high-density nonvolatile memories, sensors, or nanoscale electronic devices [61].

Besides the C-phase selenium, it is known that tellurium also has C-phase evolved from a series of helical chains [35]. Both C-phase selenium and tellurium may form 2D material with tiled helical chains, with covalent bonds along chain axis and weaker interaction across parallel chains. However, we point out that there is great difference between C-phase selenium and tellurium. As shown in figures 4(a) and (b), we defined three bond lengths  $l_1$ ,  $l_2$  and  $l_3$  of three atoms in the primitive cell. Before and after our geometry relaxation process for tellurium, the initial  $l_1 = l_2 = l_3 = 2.9$  Å become  $l_1 = l_2 = 3.0$  Å and  $l_3 = 2.8$  Å. The helical chains attract to each other with neighboring chains, thus intra-chain atoms move towards the middle position of the unit cell. On the other hand, for selenium, the uniform bond length 2.35 Å before optimization changes to  $l_1 = 2.40$  Å,  $l_2 = 2.40$  Å and  $l_3 = 2.37$  Å, which is similar to tellurium. However, the central selenium atoms are restrained to their respective chains, without being shared equally by adjacent chains. These results suggest that the 2D formation from 1D helical chains of selenium has a tendency to become a non-centrosymmetric phase. As a comparison, we also calculated the energy-displacement relationship as shown in figure 4(d). The C-Te shows a single-well potential feature and strongly hints the middle atom is stable at the center of lattice and forming centrosymmetric structure. These two structural features can be further associated with the electronic characteristics of group-VI elements. For C-phase of Se and Te, the tellurium element has more metallic character and more delocalization electrons than selenium [62]. Thus, one may understand intuitively the different behaviors of these two 2D structures.

It is interesting to find that the Dirac cone of S-Se is distorted and highly anisotropic, as also studied by Xian *et al* [63]. To obtain some deeper insight, we further plot the 3D Dirac cone formed by the valence and conduction bands in the vicinity of the Dirac point. As shown in figure 5, the linear dispersion curves of energy around the Dirac point suggest electron effective mass is zero near the Fermi level. Using the formula  $v_F = (1/\hbar)(\partial E/\partial k)$ , we calculate the Fermi velocity along the different directions to examine carrier mobility around the Dirac cone. In this formula,  $\partial E/\partial k$  is the slope

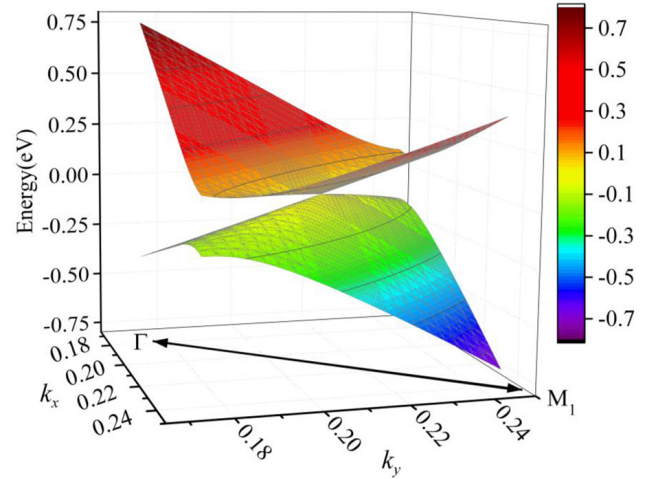


**Figure 5.** 3D Dirac cone corresponding the region indicated by the black box in figure 3(c). The double-headed arrow shows the  $\Gamma$ - $M_1$  direction, and the Fermi level is set to be zero.

of the valence or conduction band near the Dirac point, and  $\hbar$  is the reduced Planck's constant. It is well known that the Fermi velocity for graphene is  $10^6$  m s $^{-1}$  along all the directions around the Dirac point. The results of Fermi velocity indicate the electronic structure of the Dirac cone of S-Se has distinct anisotropic properties. Along the  $\Gamma$ - $M_1$  direction, our calculated Fermi velocity is  $1.26 \times 10^6$  m s $^{-1}$  from the Dirac point to  $M_1$  point, and  $v_F = 0.68 \times 10^6$  m s $^{-1}$  from the Dirac point to  $\Gamma$  point. The larger Fermi velocity is comparable to that in graphene and other 2D inorganic Dirac materials. This slope difference suggests that the Dirac cone is tilted along the  $\Gamma$ - $M_1$  direction, similar to the feature found in hydrogenated graphene [64]. Further, we calculate the Fermi velocity along the direction perpendicular to  $\Gamma$ - $M_1$  path, the result is the significantly reduced with the value of  $v_F = 0.24 \times 10^6$  m s $^{-1}$ , further confirming the anisotropic property. The intriguing band structure anisotropy creates a new tunability for electronic transport based on the S-Se materials. What is more, a recent computational work of 2D S-Se showed that the n-type doping of this Se structure reaches the maximal thermoelectric ZT value of 0.64 [65].

## Conclusions

In summary, we have explored three 2D monolayer selenene by using the PSO method in combination with first principle calculations, namely T-Se (1T-MoS $_2$ -like), C-Se (tiled 1D helical chain), and S-Se (square structure). Through performing the phonon-spectra calculations we confirm the stability of these phases and identify the degree of stability via the formation energy calculations. The band structure calculations show that both T-Se and C-Se have an indirect band gap of 0.71 eV and 1.74 eV. Additionally, we used the hybrid HSE06 functional to find band gaps of T-Se and C-Se are 1.11 eV and 2.64 eV respectively, which provide great opportunity of application in optoelectronic field. Further, for C-Se we find its spontaneous in-plane ferroelectric polarization to be  $2.68 \times 10^{-10}$  C m $^{-1}$  per layer, with the barrier height of its

double-well potential of 271 meV per unit cell. This allows us to design nonvolatile sensors and nanoscale electronic devices at an atomistic scale using the ferroelectric property. Moreover, S-Se has a Dirac point, with a band gap of 0.11 eV when including the spin-orbit coupling. We present the 3D dispersion and Fermi velocity around the Dirac point to demonstrate its tilted and anisotropic features. All these investigated structures show a variety of promising application perspectives of 2D selenium materials [66].

## Acknowledgments

This work was supported by the National Natural Science Foundation of China (Grants No. 51672171, No. 11804216, No. 51861145315 and No. 5181101790), the National Key Basic Research Program of China (Grant No. 2015CB921600), the fund of the State Key Laboratory of Solidification Processing in NWP (SKLSP201703) and the Eastern Scholar Program from the Shanghai Municipal Education Commission. Special Program for Applied Research on Super Computation of the NSFC-Guangdong Joint Fund (the second phase), the supercomputing services from AM-HPC, the China Postdoctoral Science Foundation, the China Scholarship Council, and the Fok Ying Tung Education Foundation are also acknowledged. TH and WR also acknowledge the Young Scientist exchange program supported by Ministry of Science and Technology of China and National Research Foundation of Korea.

## ORCID iDs

Chao Liu  <https://orcid.org/0000-0002-7774-9111>

Tao Hu  <https://orcid.org/0000-0002-3293-0881>

Heng Gao  <https://orcid.org/0000-0003-3830-3261>

Wei Ren  <https://orcid.org/0000-0001-7317-3867>

## References

- [1] Novoselov K S, Jiang D, Schedin F, Booth T J, Khotkevich V V, Morozov S V and Geim A K 2005 Two-dimensional atomic crystals *Proc. Natl Acad. Sci. USA* **102** 10451
- [2] Castro Neto A H, Guinea F, Peres N M R, Novoselov K S and Geim A K 2009 The electronic properties of graphene *Rev. Mod. Phys.* **81** 109
- [3] Miro P, Audiffred M and Heine T 2014 An atlas of two-dimensional materials *Chem. Soc. Rev.* **43** 6537
- [4] Fu X, Li F, Lin J F, Gong Y, Huang X, Huang Y, Han B, Zhou Q and Cui T 2017 Pressure-dependent light emission of charged and neutral excitons in monolayer MoSe<sub>2</sub> *J. Phys. Chem. Lett.* **8** 3556
- [5] Ferrari A C et al 2006 Raman spectrum of graphene and graphene layers *Phys. Rev. Lett.* **97** 187401
- [6] Splendiani A, Sun L, Zhang Y B, Li T S, Kim J, Chim C Y, Galli G and Wang F 2010 Emerging photoluminescence in monolayer MoS<sub>2</sub> *Nano Lett.* **10** 1271
- [7] Chiriacescu C, Cahill D G, Nguyen N, Johnson D, Bodapati A, Keblinski P and Zschack P 2007 Ultralow thermal conductivity in disordered, layered WSe<sub>2</sub> crystals *Science* **315** 351
- [8] Kang J, Zhang L and Wei S H 2016 A unified understanding of the thickness-dependent bandgap transition in hexagonal two-dimensional semiconductors *J. Phys. Chem. Lett.* **7** 597
- [9] Mannix A J et al 2015 Synthesis of borophenes: anisotropic, two-dimensional boron polymorphs *Science* **350** 1513
- [10] Liu H, Neal A T, Zhu Z, Luo Z, Xu X F, Tomanek D and Ye P D 2014 Phosphorene: an unexplored 2D semiconductor with a high hole mobility *ACS Nano* **8** 4033
- [11] Vogt P, De Padova P, Quaresima C, Avila J, Frantzeskakis E, Asensio M C, Resta A, Ealet B and Le Lay G 2012 Silicene: compelling experimental evidence for graphenelike two-dimensional silicon *Phys. Rev. Lett.* **108** 155501
- [12] Karmakar S, Chowdhury C and Datta A 2018 Noble-metal-supported GeS monolayer as promising single-atom catalyst for CO oxidation *J. Phys. Chem. C* **122** 14488
- [13] Zolyomi V, Drummond N D and Fal'ko V I 2014 Electrons and phonons in single layers of hexagonal indium chalcogenides from *ab initio* calculations *Phys. Rev. B* **89** 205416
- [14] Debbichi L, Eriksson O and Lebegue S 2015 Two-dimensional indium selenides compounds: an *ab initio* study *J. Phys. Chem. Lett.* **6** 3098
- [15] Naguib M, Come J, Dyatkin B, Presser V, Taberna P L, Simon P, Barsoum M W and Gogotsi Y 2012 MXene: a promising transition metal carbide anode for lithium-ion batteries *Electrochem. Commun.* **16** 61
- [16] Dall'Agnese Y, Taberna P L, Gogotsi Y and Simon P 2015 Two-dimensional vanadium carbide (MXene) as positive electrode for sodium-ion capacitors *J. Phys. Chem. Lett.* **6** 2305
- [17] Wang Q H, Kalantar-Zadeh K, Kis A, Coleman J N and Strano M S 2012 Electronics and optoelectronics of two-dimensional transition metal dichalcogenides *Nat. Nanotechnol.* **7** 699
- [18] Kan E, Li M, Hu S, Xiao C, Xiang H and Deng K 2013 Two-dimensional hexagonal transition-metal oxide for spintronics *J. Phys. Chem. Lett.* **4** 1120
- [19] Osada M and Sasaki T 2012 Two-dimensional dielectric nanosheets: novel nanoelectronics from nanocrystal building blocks *Adv. Mater.* **24** 210
- [20] Zhang C, Jiao Y, He T, Bottle S, Frauenheim T and Du A 2018 Predicting two-dimensional C<sub>3</sub>B/C<sub>3</sub>N van der Waals p-n heterojunction with strong interlayer electron coupling and enhanced photocurrent *J. Phys. Chem. Lett.* **9** 858
- [21] Bonaccorso F, Colombo L, Yu G H, Stoller M, Tozzini V, Ferrari A C, Ruoff R S and Pellegrini V 2015 Graphene, related two-dimensional crystals, and hybrid systems for energy conversion and storage *Science* **347** 1246501
- [22] Penev E S, Kutana A and Yakobson B I 2016 Can two-dimensional boron superconduct? *Nano Lett.* **16** 2522
- [23] Balog R et al 2010 Bandgap opening in graphene induced by patterned hydrogen adsorption *Nat. Mater.* **9** 315
- [24] Doganov R A et al 2015 Transport properties of pristine few-layer black phosphorus by van der Waals passivation in an inert atmosphere *Nat. Commun.* **6** 6647
- [25] Zhu Z, Guan J, Liu D and Tomanek D 2015 Designing isoelectronic counterparts to layered group V semiconductors *ACS Nano* **9** 8284
- [26] Ma F, Jiao Y, Gao G, Gu Y, Bilic A, Chen Z and Du A 2016 Graphene-like two-dimensional ionic boron with double dirac cones at ambient condition *Nano Lett.* **16** 3022
- [27] Cui Z H, Jimenez-Izal E and Alexandrova A N 2017 Prediction of two-dimensional phase of boron with anisotropic electric conductivity *J. Phys. Chem. Lett.* **8** 1224
- [28] Fleurence A, Friedlein R, Ozaki T, Kawai H, Wang Y and Yamada-Takamura Y 2012 Experimental evidence for epitaxial silicene on diboride thin films *Phys. Rev. Lett.* **108** 245501
- [29] Dávila M E, Xian L, Cahangirov S, Rubio A and Le Lay G 2014 Germanene: a novel two-dimensional germanium



- allotrope akin to graphene and silicene *New J. Phys.* **16** 095002
- [30] Xu Y, Yan B, Zhang H J, Wang J, Xu G, Tang P, Duan W and Zhang S C 2013 Large-gap quantum spin Hall insulators in tin films *Phys. Rev. Lett.* **111** 136804
- [31] Özçelik V O, Aktürk O Ü, Durgun E and Ciraci S 2015 Prediction of a two-dimensional crystalline structure of nitrogen atoms *Phys. Rev. B* **92** 125420
- [32] Kou L, Ma Y, Tan X, Frauenheim T, Du A and Smith S 2015 Structural and electronic properties of layered arsenic and antimony arsenide *J. Phys. Chem. C* **119** 6918
- [33] Aktürk O Ü, Özçelik V O and Ciraci S 2015 Single-layer crystalline phases of antimony: antimonenes *Phys. Rev. B* **91** 235446
- [34] Pumera M and Sofer Z 2017 2D monoelemental arsenene, antimonene, and bismuthene: beyond black phosphorus *Adv. Mater.* **29** 1605299
- [35] Zhu Z L et al 2017 Multivalency-driven formation of Te-based monolayer materials: a combined first-principles and experimental study *Phys. Rev. Lett.* **119** 106101
- [36] Liang F X and Qian H S 2009 Synthesis of tellurium nanowires and their transport property *Mater. Chem. Phys.* **113** 523
- [37] Song J M, Lin Y Z, Zhan Y J, Tian Y C, Liu G and Yu S H 2008 Superlong high-quality tellurium nanotubes: synthesis, characterization, and optical property *Cryst. Growth Des.* **8** 1902
- [38] Qin J K et al 2017 Controlled growth of a large-size 2D selenium nanosheet and its electronic and optoelectronic applications *ACS Nano* **11** 10222
- [39] Wang Y, Lv J, Zhu L and Ma Y 2010 Crystal structure prediction via particle-swarm optimization *Phys. Rev. B* **82** 094116
- [40] Kresse G and Furthmüller J 1996 Efficiency of *ab initio* total energy calculations for metals and semiconductors using a plane-wave basis set *Comput. Mater. Sci.* **6** 15
- [41] Kresse G and Furthmüller J 1996 Efficient iterative schemes for *ab initio* total-energy calculations using a plane-wave basis set *Phys. Rev. B* **54** 11169
- [42] Perdew J P, Burke K and Ernzerhof M 1996 Generalized gradient approximation made simple *Phys. Rev. Lett.* **77** 3865
- [43] Blöchl P E 1994 Projector augmented-wave method *Phys. Rev. B* **50** 17953
- [44] Kresse G and Joubert D 1999 From ultrasoft pseudopotentials to the projector augmented-wave method *Phys. Rev. B* **59** 1758
- [45] Heyd J, Scuseria G E and Ernzerhof M 2003 Hybrid functionals based on a screened coulomb potential *J. Chem. Phys.* **118** 8207
- [46] Heyd J, Scuseria G E and Ernzerhof M 2006 Erratum: 'Hybrid functionals based on a screened Coulomb potential' (2003 *J. Chem. Phys.* **118** 8207) *J. Chem. Phys.* **124** 219906
- [47] Tkatchenko A and Scheffler M 2009 Accurate molecular van der Waals interactions from ground-state electron density and free-atom reference data *Phys. Rev. Lett.* **102** 073005
- [48] Togo A, Oba F and Tanaka I 2008 First-principles calculations of the ferroelastic transition between rutile-type and  $\text{CaCl}_2$ -type  $\text{SiO}_2$  at high pressures *Phys. Rev. B* **78** 134106
- [49] Togo A and Tanaka I 2015 First principles phonon calculations in materials science *Scr. Mater.* **108** 1
- [50] Xing C, Xie Z, Liang Z, Liang W, Fan T, Ponraj J S, Dhanabalan S C, Fan D and Zhang H 2017 2D nonlayered selenium nanosheets: facile synthesis, photoluminescence, and ultrafast photonics *Adv. Opt. Mater.* **5** 1700884
- [51] Liu D, Lin X and Tomanek D 2018 Microscopic mechanism of the helix-to-layer transformation in elemental group VI solids *Nano Lett.* **18** 4908
- [52] Tran H D, Amsler M, Botti S, Marques M A and Goedecker S 2014 First-principles predicted low-energy structures of  $\text{NaSc}(\text{BH}_4)_4$  *J. Chem. Phys.* **140** 124708
- [53] Voss J, Hummelshøj J S, Lodziana Z and Vegge T 2009 Structural stability and decomposition of  $\text{Mg}(\text{BH}_4)_2$  isomorphs—an *ab initio* free energy study *J. Phys.: Condens. Matter.* **21** 012203
- [54] Bludau W, Onton A and Heinke W 1974 Temperature dependence of the band gap of silicon *J. Appl. Phys.* **45** 1846
- [55] Tang W, Sanville E and Henkelman G 2009 A grid-based Bader analysis algorithm without lattice bias *J. Phys.: Condens. Matter.* **21** 084204
- [56] Henkelman G, Uberuaga B P and Jonsson H 2000 A climbing image nudged elastic band method for finding saddle points and minimum energy paths *J. Chem. Phys.* **113** 9901
- [57] Henkelman G and Jónsson H 2000 Improved tangent estimate in the nudged elastic band method for finding minimum energy paths and saddle points *J. Chem. Phys.* **113** 9978
- [58] King-Smith R D and Vanderbilt D 1993 Theory of polarization of crystalline solids *Phys. Rev. B* **47** 1651
- [59] Resta R 1992 Theory of the electric polarization in crystals *Ferroelectrics* **136** 51
- [60] Xiao C, Wang F, Yang S A, Lu Y, Feng Y and Zhang S 2018 Elemental Ferroelectricity and Antiferroelectricity in Group-V Monolayer *Adv. Funct. Mater.* **28** 1707383
- [61] Nuraje N and Su K 2013 Perovskite ferroelectric nanomaterials *Nanoscale* **5** 8752
- [62] Liu Y, Wu W and Goddard W A 3rd 2018 Tellurium: fast electrical and atomic transport along the weak interaction direction *J. Am. Chem. Soc.* **140** 550
- [63] Xian L, Pérez Paz A, Bianco E, Ajayan P M and Rubio A 2017 Square selenene and tellurene: novel group VI elemental 2D materials with nontrivial topological properties *2D Mater.* **4** 041003
- [64] Lu H-Y, Cuamba A S, Lin S-Y, Hao L, Wang R, Li H, Zhao Y and Ting C S 2016 Tilted anisotropic Dirac cones in partially hydrogenated graphene *Phys. Rev. B* **94** 195423
- [65] Lin C, Cheng W, Chai G and Zhang H 2018 Thermoelectric properties of two-dimensional selenene and tellurene from group-VI elements *Phys. Chem. Chem. Phys.* **20** 24250
- [66] Ren W, Ye J-T, Shi W, Tang Z-K, Chan C T and Sheng P 2009 Negative compressibility of selenium chains confined in the channels of  $\text{AlPO}_4\cdot 5$  single crystals *New J. Phys.* **11** 103014